

DPN: Detail-Preserving Network with High Resolution Representation for Efficient Segmentation of Retinal Vessels

Song Guo

Received: date / Accepted: date

Abstract Retinal vessels are important biomarkers for many ophthalmological and cardiovascular diseases. Hence, it is of great significance to develop automatic models for computer-aided diagnosis. Existing methods, such as U-Net follows the encoder-decoder pipeline, where detailed information is lost in the encoder in order to achieve a large field of view. Although spatial detailed information could be recovered partly in the decoder, while there is noise in the high-resolution feature maps of the encoder. And, we argue this encoder-decoder architecture is inefficient for vessel segmentation. In this paper, we present the detail-preserving network (DPN), which avoids the encoder-decoder pipeline. To preserve detailed information and learn structural information simultaneously, we designed the detail-preserving block (DP-Block). Further, we stacked eight DP-Blocks together to form the DPN. More importantly, there are no down-sampling operations among these blocks. Therefore, the DPN could maintain a high/full resolution during processing, avoiding the loss of detailed information. To illustrate the effectiveness of DPN, we conducted experiments over three public datasets. Experimental results show, compared to state-of-the-art methods, DPN shows competitive/better performance in terms of segmentation accuracy, segmentation speed, and model size. Specifically, 1) Our method achieves comparable segmentation performance on the DRIVE, CHASE_DB1, and HRF datasets. 2) The segmentation speed of DPN is over 20-160 \times faster than other methods on the DRIVE dataset. 3) The number of parameters of DPN is around 120k, far less than all comparison methods.

This work is supported by PhD research startup foundation of Xi'an University of Architecture and Technology (No.1960320048).

Song Guo
School of Information and Control Engineering, Xi'an University of Architecture and Technology, Xi'an 710055, China
E-mail: guomugong@hotmail.com

Keywords Retinal Vessel Segmentation · High Resolution Representation · Fast Speed · Fundus Image

1 Introduction

Retinal blood vessels are an important part of fundus images, and they can be applied to the diagnosis of many ophthalmological diseases, such as diabetic retinopathy (Wong et al., 2018), cataract (Cao et al., 2020), and hypertensive retinopathy (Irshad and Akram, 2014). Specifically, when patients with diffuse choroidal hemangioma, retinal blood vessels will expand (Scott et al., 1999). Vascular structures in patients with cataracts are unclear or even invisible (Cao et al., 2020). In addition, as retinal blood vessels and cerebral blood vessels are similar in anatomical, physiological, and embryological characteristics, so that retinal vessels are also important biomarkers to some cardiovascular diseases (Wong et al., 2004; Schmidt-Erfurth et al., 2018). Accurate segmentation of blood vessels is the basic step of efficient computer-aided diagnosis (CAD). However, manual segmentation of retinal vessels is time-consuming and relies heavily on the human experience. Therefore, it is necessary to develop accurate and fast vessel segmentation methods for CAD.

Considering the clinical application scenarios, a good vessel segmentation model for CAD should satisfy the following two conditions. 1) High accuracy. The model needs to be capable to recognize both thin vessels and thick vessels, even for extremely thin vessels with one-pixel width. For example, the appearance of neovascularization can be used to diagnose and grade diabetes retinopathy (Wong et al., 2018). 2) Fast processing speed (Yu et al., 2012; Villalobos-Castaldi et al., 2010). The model needs to have a fast processing speed to meet clinical application, as faster speed means greater throughput and higher processing efficiency.

Existing vessel segmentation methods could be divided into two categories (Guo et al., 2019): unsupervised methods and supervised methods. Unsupervised methods utilize manually designed low-level features and rules (Azzopardi and Petkov, 2013; Azzopardi et al., 2015; Srinidhi et al., 2018), therefore, they show poor extensibility. Supervised methods utilize human annotated training images, and their segmentation accuracy is usually higher than that of unsupervised methods (Schmidt-Erfurth et al., 2018). Deep learning-based supervised methods could learn high-level features in an end-to-end manner, and they show superior performance in terms of segmentation accuracy and extensibility (Jin et al., 2019; Yan et al., 2018b). Most deep vessel segmentation models follow the architecture of the fully convolutional network (FCN) (Shelhamer et al., 2017), in which the resolution of features is first down-sampled and then up-sampled to generate pixel-wise segmentation maps. However, the detailed information is lost in FCN. Furthermore, a U-Net (Ronneberger et al., 2015) model was proposed, which could utilize intermediate layers in the up-sampling path to fuse more spatial information to generate fine segmentation maps. Although the detailed information could

be utilized in the U-Net, the extra noise was also introduced. Moreover, most U-Net variant models (Jim et al., 2019) require multiple forward passes to generate a segmentation map for one testing image, since they split one fundus image into hundreds of small patches. As a result, they show slow segmentation speed and the contextual information is not fully utilized.

Different from U-Net that recovering the spatial details in the decoder to achieve a high-resolution representation, in this paper, we present a deep model termed detail-preserving network (DPN) which could preserve a high-resolution representation all the time. Inspired by HRNet (Wang et al., 2020), the DPN learns the full-resolution representation directly rather than the low-resolution representation. In this manner, the DPN could locate the boundaries of thin vessels accurately. To this end, on one hand, we present the detail-preserving block (DP-Block), where multi-scale features are fused in a cascaded manner so that more contextual information could be utilized. And, the resolution of input features and output features of DP-Block is never changed, so that the detailed spatial information could be preserved. On the other hand, we stacked eight DP-Blocks together to form the DPN. We note that there are no down-sampling operations among these DP-Blocks so that the DPN could learn both semantic features via a large field of view and preserve the detailed information simultaneously. To validate the effectiveness of our method, we conducted experiments on the DRIVE, CHASE_DB1, and HRF datasets. Experimental results reveal that our method shows competitive/better performance compared with other state-of-the-art methods.

Overall, our contributions are summarized as follows.

1. We present the detail-preserving block, which could learn the structural information and preserve the detailed information via intra-block multi-scale fusion.
2. We present the detail-preserving network, which mainly consists of eight serially connected DP-Blocks, and it maintains high-resolution representations during the whole process. As a result, the DPN could learn both semantic features and preserve the detailed information simultaneously.
3. We conducted experiments over three public datasets. Experimental results reveal that our method achieves comparable or even superior performance over other methods in terms of segmentation accuracy, segmentation speed, and model size.

The rest of this paper is organized as follows. Related works about vessel segmentation are introduced in Section 2. Our method is described in Section 3. Experimental results are analyzed in Section 4. Conclusions are drawn in Section 5.

2 Related Works

Retinal vessel segmentation is a pixel-wise binary classification problem, and the objective is to locate each vessel pixel accurately for further processing.

According to whether annotations are used, existing methods could be divided into two categories: unsupervised methods and supervised methods.

2.1 Unsupervised Methods

Unsupervised methods usually utilize human-designed low-level features, such as edge, line, and color. Manually annotated information is not utilized. Unsupervised methods can be roughly divided into match filter based method (Wang et al., 2013; Azzopardi et al., 2015), vessel tracking based method (Yin et al., 2012), threshold based method (Li et al., 2006; Saleh et al., 2011) and morphology based method (Garg et al., 2007; Wang et al., 2019b).

Wang et al. (Wang et al., 2013) proposed a multi-stage method for vessel segmentation. In their method, a matched filtering was first adopted for vessel enhancing, and then vessels were located via a multi-scale hierarchical decomposition. Yin et al. (Yin et al., 2012) proposed a vessel tracking method, in which local grey information was utilized to select vessel edge points. Then a Bayesian method was used to determine the direction of vessels. Garg et al. (Garg et al., 2007) proposed a curvature-based method. In their method, the vessel lines were first extracted using curvature information, and then a region growing method was used to generate the whole vessel tree. Li et al. (Li et al., 2006) proposed an adaptive threshold method for vessel segmentation, and their method could detect both large and small vessels. Christodoulidis et al. (Christodoulidis et al., 2016) utilized line detector and tensor voting for vessel segmentation, and thin vessels were well detected.

A major limitation of the unsupervised method is that the features and rules are designed by a human. It is hard to design a satisfactory feature that works well on large-scale fundus images. This kind of method may show poor generalization ability.

2.2 Supervised Methods

In contrast to unsupervised methods, supervised methods need annotation information to build vessel segmentation models. Before deep learning methods were applied to vessel segmentation, supervised methods usually consist of two procedures: feature extraction and classification. In the first procedure, features were extracted by human-designed rules, just as that did in unsupervised methods. In the second procedure, supervised classifiers were employed to classify these extracted features into vessels or non-vessels. As deep learning methods unify feature extraction and classification procedures together, they could extract much discriminative features.

Deep learning-based methods could be roughly divided into classification-based methods and segmentation-based methods (Srinidhi et al., 2017; Mookiah et al., 2020). For classification-based methods, the category for each pixel is determined by its surrounding small image patch (Liskowski and Krawiec, 2016;

Wang et al., 2019c). This kind of method does not make full use of contextual information. For segmentation-based methods, existing methods follow the architecture of FCN, where the resolution of feature maps are first down-sampled to encode structural information, and then the resolution of feature maps are up-sampled further to generate pixel-wise segmentation maps. Although successive down-sampling operations could reduce the model’s computational complexity and increase the model’s receptive field, it inevitably loses detailed information. As a result, this kind of method shows poor performance in the segmentation of thin/tiny blood vessels. To alleviate this problem, multi-scale fusion methods and graph models were adopted. For instance, Maninis et al. (Maninis et al., 2016) proposed a FCN for vessel segmentation. They adopted a multi-scale feature fusion to generate fine vessel maps. Fu et al. (Fu et al., 2016) adopted a holistically-nested edge detection model (Xie and Tu, 2017) to generate coarse segmentation maps, and then a conditional random field was adopted to model the relationship among long-range pixels to refine segmentation maps. Besides above methods, Ronneberger et al. proposed an u-shape network, called U-Net to preserve spatial information (Ronneberger et al., 2015). Similar to FCN, the feature maps were first down-sampled to a low resolution, then they were up-sampled step-by-step. In each step, the intermediate features with high representation in the encoder were utilized. Several methods based on U-Net have been proposed for vessel segmentation. For instance, Jin et al. (Jin et al., 2019) proposed a DUNet for vessel segmentation. They used deformable convolution rather than grid convolution in U-Net to capture the shape of vessels. Wu et al. (Wu et al., 2018) designed a two-branch network, where each branch consists of two U-Nets. The output of their method was the average of the predictions of these two branches. In addition, different from (Maninis et al., 2016) and (Fu et al., 2016) that used the entire image as training samples. Both (Jin et al., 2019) and (Wu et al., 2018) used overlapped image patches of size 48×48 as training samples, and a re-composed procedure is required to complete a segmentation map during testing. Hence, they suffer from a high computation complexity. Despite their success, the problem of losing spatial information in the down-sampling phase has not been fully addressed. Meantime, considering both computation complexity and segmentation accuracy, there still lacks a fast and accurate vessel segmentation model.

3 Our Method

In this section, we will describe our method in detail, including the architecture of our proposed detail-preserving network, the detail-preserving block, and the loss function at last.

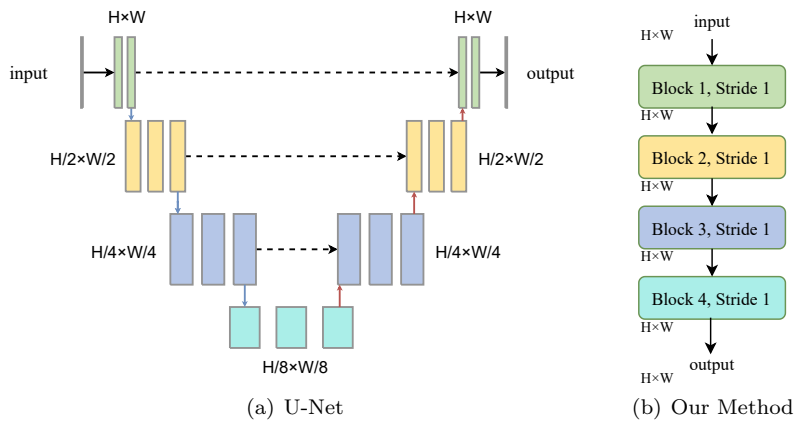


Fig. 1 (a) The architecture of U-Net (Ronneberger et al., 2015). The resolution of feature maps is first decreased in the encoder, and then up-scaled in the decoder (H and W denote the height and width of feature maps). (b) The architecture of the proposed DPN, in which high-resolution representations are learned.

3.1 Detail-Preserving Network

A good vessel segmentation model should segment both thick vessels and thin vessels, this requires the segmentation model to learn structural semantic information and preserve detailed spatial information simultaneously. The structural information is beneficial to locate thick vessels, and it requires the model to have a large field of view. While the detailed spatial information is important to locate vessel boundaries accurately, especially for thin vessels. However, it is easy to lose detailed information when learning structural information. For example, the structural information of U-Net (Ronneberger et al., 2015) is learned by successive down-sampling operations, and the resolution of feature maps is decreased by a factor of 8 or even more (as can be seen in Fig. 1(a)). Such low resolution implies that the spatial information of thin vessels is lost. U-Net utilizes intermediate features of the encoder to recover the spatial information. However, intermediate feature maps of the encoder may have noise (non-vessel pixels are highlighted) due to a small field of view.

Our study is motivated by whether it is possible to preserve detailed information, while the network has a large field of view. To this end, we present a high representation network, called detail-preserving network for vessel segmentation. The architecture of our model is visualized in Fig. 2.

We can observe from Fig. 2 that DPN mainly consists of three parts: the front convolution operation, eight detail-preserving blocks, and four loss functions (including three supervision losses). Compared with other vessel segmentation models, the DPN has the following characteristics. 1) Different from U-Net, there are no down-sampling operations among these DP-Blocks, this implies the resolution of features among these DP-Blocks keeps the same. In

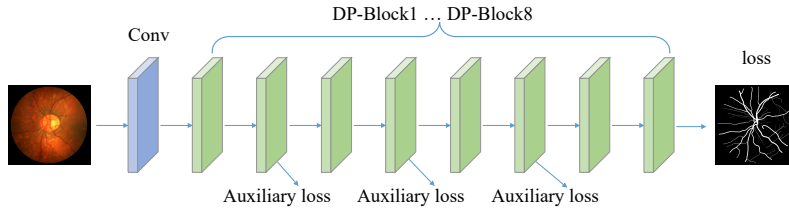


Fig. 2 Overview of the proposed detail-preserving network. DPN consists of one convolutional layer and eight DP-Blocks, and it maintains high/full resolution representations during the whole process. Meantime, we add three auxiliary losses to pass extra gradient signals.

other words, the DPN maintains a full-resolution representation during the whole processing (from input to output), thereby it could preserve detailed spatial information. 2) For DP-Block, the receptive field of the output neuron could be as large as four times that of the input neuron, while the detailed information could also be preserved. Therefore, DPN could obtain a large field of view through stacking multiple DP-Blocks. Moreover, a large field of view means that DPN could learn semantic information instead of local information. The architecture of the DP-Block will be described in the next section. 3) Different from U-Net that utilized VGGNet or ResNet as the backbone, which incurs a large number of parameters. The total number of parameters of DPN is less than 120k. 4) The input of DPN is the entire image so that it could integrate more contextual information than patch-level segmentation models. Meantime, our method only needs one forward pass to generate the complete segmentation maps, thereby the inference speed of our method is faster than patch-level models.

Relationship with HRNet (Wang et al., 2020). Both DPN and HRNet learn a high-resolution representation, while there are some differences. 1) Proposed DPN only maintains one kind of resolution, i.e., the high-resolution stream (as can be seen in Fig. 1), and multi-scale feature fusion is employed in DP-Blocks. While HRNet maintains multi-streams with different resolutions and multi-scale fusion is employed among these streams. 2) The method for multi-scale feature fusion is different. Proposed DPN fuses low-resolution feature maps with high-resolution feature maps in a step-by-step manner. While in HRNet, the representations with different resolutions are concatenated directly.

3.2 Detail-Preserving Block

DP-Block as the key component of DPN, could learn structural semantic information and preserve the spatial detailed information at the same time. Overview of the DP-Block is visualized in Fig. 3. We can observe that the input feature of the DP-Block is fed into three branches, and each branch is processed in different scales. The output feature of the DP-Block is obtained

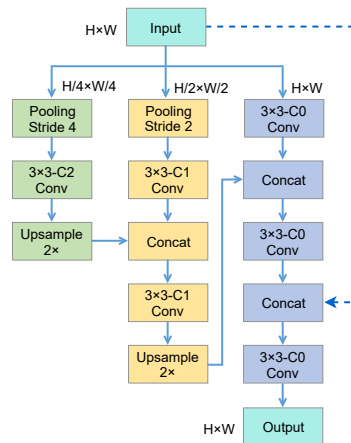


Fig. 3 Overview of the proposed detail-preserving block, where C0, C1, and C2 denote the number of convolutional filters for each branch.

by fusing features of three scales. The computing procedure of the DP-Block is as follows.

For the first branch, a convolution operation with 3×3 kernel was adopted to learn detailed information. For the second branch, a pooling operation with stride 2 was adopted, then the resolution of feature maps was down-sampled by a factor of 2. A convolution operation with 3×3 kernel was adopted further. For the third branch, it was used to enlarge the field of view and learn structural information. In this branch, a pooling operation with stride 4 was first adopted, as a result, the resolution of feature maps was down-sampled by a factor of 4 and the receptive field was increased by a factor of 4 either. A convolution operation with 3×3 kernel was then adopted to extract features. The extracted features of each branch were fused in a cascaded manner. Specifically, features learned by the third branch were first up-sampled $2 \times$, and then connected to the second branch, and the output of the second branch was further connected to the first branch. Here, we used a concatenation operation for feature fusion. The whole procedure is summarized in Alg 1. We note that the resolution of the output feature of the DP-Block is the same as the input feature so that the DP-Block could not only preserve detailed information but also learns multi-scale features.

Number of parameters. In our experiments, the number of convolutional filters C0, C1, and C2 for each branch of DP-Block was set to 16, 8, and 8, respectively. In DPN, the dimension of the output feature of the first convolution operation is $H \times W \times 32$, then the number of parameters of the first DP-Block is 21,704. For the second to the last DP-Block, the dimension of the input feature is $H \times W \times 16$, then the number of parameters for each DP-Block is only 13,896. Hence, the total number of parameters of the DPN is less than 120k. Experimental results show that the DPN could be effectively learned from scratch with limited training samples.

Algorithm 1: Description of the DP-Block.**Input:** Feature map X **Output:** Feature map Y

$$x1 = \delta(k1 * X);$$

$$x2 = \delta(k2 * \text{maxpool}(X, 2));$$

$$x3 = \delta(k3 * \text{maxpool}(X, 4));$$

$$x4 = \delta(k4 * \text{concat}(x2, \text{deconv}(x3, 2)));$$

$$x5 = \delta(k5 * \text{concat}(x1, \text{deconv}(x4, 2)));$$

$$Y = \delta(k6 * \text{concat}(x5, X));$$

In the above formulas, δ refers to ReLU function, $*$ denotes convolution operation, k_i denotes convolutional filters with kernel size 3×3 , maxpool denotes max pooling, deconv denotes deconvolution operation to upscale the feature map, and concat denotes concatenation operation on the channel dimension.

Relationship with Inception Module. Different from the inception module (Szegedy et al., 2015) that uses parallel convolution operations with different convolutional kernels to learn multi-scale features, our DP-Block adopts down-sampling first, so that the receptive field is further enlarged. The receptive field of each output neuron is four times that of the input neuron. As a result, the receptive field grows exponentially when stacking multiple DP-Blocks. Furthermore, rather than parallel processing branches in the inception module, the features of different branches were fused in a cascaded manner in DP-Block to better learn multi-scale features.

3.3 Loss Function

Blood vessels account only for a small proportion of the entire image. Specifically, the proportion of vessels is 8.69%/6.93%/7.71% on the DRIVE/CHASE_DB1/HRF datasets, respectively. There exists a class imbalance problem in vessel segmentation. To solve this problem, we adopted class balanced cross-entropy loss (Xie and Tu, 2017), which uses a weight factor to balance vessel pixels and non-vessel pixels. The class-balanced cross-entropy loss is defined as follows.

$$L(p, y|\theta) = -\beta \sum_{y_j=1} \log p_j - (1 - \beta) \sum_{y_j=0} \log (1 - p_j) \quad (1)$$

where p is a probability map obtained by a sigmoid operation, and p_j denotes the probability that the j^{th} pixel belongs to vessel. In addition, y denotes the ground truth, and θ denotes model parameters. Rather than using a fixed value, the weight factor β is calculated at each iteration based on the distribution of vessel pixels and non-vessel pixels. The weight factor β is defined as below.

$$\beta = \frac{N_-}{N_+ + N_-} \quad (2)$$

where N_+ denotes the number of vessel pixels, and N_- denotes the number of non-vessel pixels. Since $N_- > N_+$, the weight for vessel pixels is large than

the weight for non-vessel pixels. So that the model would focus more on vessel pixels than non-vessel pixels.

Besides the segmentation loss after the last layer of DPN, we add three auxiliary losses to the intermediate layers of DPN to pass extra gradient signals to alleviate the gradient-vanish problem, just as that did in DSN (Lee et al., 2015) and GoogLeNet (Szegedy et al., 2015). As can be seen in Fig. 2, the first auxiliary loss is after DP-Block2, the second auxiliary loss is after the DP-Block4, and the last one is after the DP-Block6. The segmentation loss is connected after the DP-Block8. Taking the first auxiliary loss as an example, we first adopted a convolution operation with one 1×1 filter to the output features of DP-Block2, then a feature map with one channel was obtained. At last, this feature map was fed into the class balanced cross-entropy loss function.

Hence, the overall objective function of DPN is the sum of three auxiliary losses and one segmentation loss, and it can be formulated as follows.

$$L_{all}(x, y|\theta) = \sum_{i=1}^4 L(p^i(x), y|\theta) + \frac{\lambda}{2} \|\theta\|^2 \quad (3)$$

where p^i denotes the probability map of the i^{th} loss function, and λ denotes the weight decay coefficient.

In conclusion, we aim to minimize the above objective function during training. In the test phase, the output of the last segmentation loss is taken as the segmentation results of DPN, and the segmentation probability maps of auxiliary losses are ignored.

4 Experiments

4.1 Materials

Performances of our method were evaluated on three public datasets: DRIVE (Staal et al., 2004), CHASE_DB1 (Fraz et al., 2012), and HRF (Budai et al., 2013).

The DRIVE (Digital Retinal Images for Vessel Extraction) dataset contains 40 color fundus images captured with a 45° FOV (Field of View). Each image has the same resolution, which is 565×584 (width \times height). The dataset is partitioned into the training set and the test set officially, and each set contains 20 images. For the test set, two groups of annotations are provided. We used the annotation of the first group as ground-truth to evaluate our model, just as other methods did. In addition, the FOV masks for calculating evaluation metrics are also provided.

The CHASE_DB1 dataset contains 28 fundus images (999×960) captured with a 30° FOV. As the split of the training set and the test set is not provided. For a fair comparison with other methods, we did two sets of experiments. We adopted a 20/8 partition for the first set of experiments, where the first 20

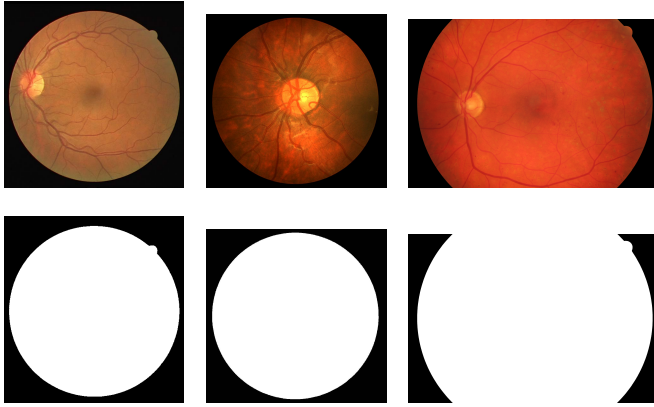


Fig. 4 Fundus images (the first row) and the corresponding FOV masks (the second row) from DRIVE, CHASE_DB1 and HRF datasets, from left to right.

images were selected for training and the rest 8 images for testing. For another set of experiments, we adopted a 14/14 (training/test) partition.

The HRF (High Resolution Fundus) dataset contains 45 high-resolution fundus images, with resolution 2336×3504 . Among 45 images, 15 images are with diabetic retinopathy, 15 images are with glaucoma and the rest 15 images are healthy. As no partition of the training set and test set available, in our experiments, we used the first 15 images as the training set and the rest 30 images for evaluation. Besides, the FOV masks are provided in HRF.

As the FOV masks are not present in the CHASE_DB1 dataset, we created the masks manually. The FOV masks on these three datasets are presented in Fig. 4.

4.2 Image Preparation

We use raw color fundus images to train our model, image enhancement methods like CLAHE are not adopted. Therefore, a time-consuming pre-processing procedure could be avoided when inference and the segmentation speed of our model could be further improved.

Considering that there are limited annotated training samples on the DRIVE, CHASE_DB1, and HRF, and there are no pre-training weights available. To avoid over-fitting and promote the segmentation accuracy, several transformations have been adopted to augment the training set, including flipping (horizontal and vertical) and rotation (22° , 45° , 90° , 135° , 180° , 225° , 270° , 315°). Rotated images can be seen in Fig. 5. As a result, the training images were augmented by a factor of 10 offline, and there are 220/220/165 training images in total on the DRIVE/CHASE_DB1/HRF datasets, respectively. Moreover, the training image was randomly mirrored during training for each iteration.

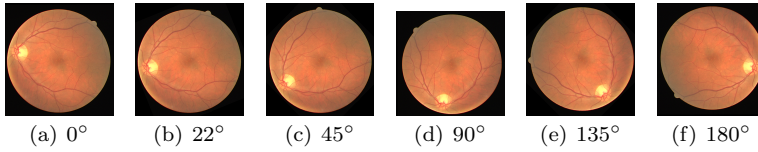


Fig. 5 Example of training images after rotating different angles.

On the DRIVE and CHASE_DB1 datasets, it is possible to feed an entire image into GPU memory. However, it is hard to feed an image sampled from HRF into GPU memory, since its resolution is as high as 2336×3504 . To deal with this problem, we scale these images from HRF to a low-resolution with size 600×900 to make sure they can be loaded into GPU memory.

4.3 Training Details

Our model was implemented based on an open-source deep learning framework *Caffe* (Jia et al., 2014), and it ran on a workstation equipped with one NVIDIA RTX 2080ti GPU.

We initialized weights of our model using xavier (Glorot and Bengio, 2010). The learning rate was initialized to $1e-3$. And we trained our model for 100k/100k/70k iterations with ADAM (Kingma and Ba, 2015) (batch size 1) using weight decay 0.0005 on the DRIVE/CHASE_DB1/HRF datasets, respectively.

To reduce computational complexity, each training image was cropped into $512 \times 512 / 632 \times 632 / 588 \times 588$ patches randomly during training on the DRIVE/CHASE_DB1/HRF datasets, respectively. And, the crop operation was performed via the data layer of *Caffe*. When testing, the entire fundus image is fed into the network without cropping, so that our model could generate a segmentation map with only one forward pass.

4.4 Evaluation Metrics

For a fair comparison with other methods Jin et al. (2019); Wang et al. (2019a); Maninis et al. (2016); Guo et al. (2019), we adopt five pixel-wise evaluation metrics, including Sensitivity (Se), Specificity (Sp), Accuracy (Acc), the Area Under the receiving operator characteristics Curve (AUC), and F1-score (F1) to evaluate the segmentation maps. Besides these pixel-wise evaluation metrics, we also use Structural Similarity Index Measure (SSIM) Wang et al. (2004) and Peak Signal to Noise Ratio (PSNR) to evaluate the segmentation maps. They are defined as follows.

$$Se = \frac{TP}{TP + FN} \quad (4)$$

$$Sp = \frac{TN}{TN + FP} \quad (5)$$

$$Acc = \frac{TP + TN}{TP + FN + TN + FP} \quad (6)$$

$$F1 = \frac{2 \times Pr \times Se}{Pr + Se} \quad (7)$$

where $Pr = \frac{TP}{TP + FP}$, and true positive (TP) denotes the number of vessel pixels classified correctly and true negative (TN) denotes the number of non-vessel pixels classified correctly. Similarly, false positive (FP) denotes the number of non-vessel pixels misclassified as vessels and false negative (FN) denotes the number of vessel pixels misclassified as non-vessels. To calculate Se, Sp and Acc, we select the threshold that corresponds to the optimal operating point of the receiving operator characteristics (ROC) curve to generate the binary segmentation maps from a probability map. Also, we note that TP, FN, FP and TN are counted pixel-by-pixel, and only the pixels inside the FOV mask are calculated, not the whole fundus image. The ROC curve is obtained by multiple Se versus (1-Sp) via varying threshold. AUC evaluates the segmentation probability maps not the binary maps, which is more comprehensive. The AUC ranges from 0 to 1, and the AUC of a perfect segmentation model is 1.

At last, we also report the segmentation speed of our model using fps (frames per second). The segmentation time t for each image is counted starting from reading the raw test image from the hard disk to writing the segmentation map into the hard disk. Then, $fps = 1.0/t$.

4.5 Results and Analysis

4.5.1 Compare with Existing Methods

We compared our method with several state-of-the-art deep vessel segmentation methods on three public datasets in terms of segmentation performance, segmentation speed, and the number of parameters. Comparison results were summarized in Table 1, Table 2 and Table 3.

Segmentation performance. On the DRIVE dataset, as we can see from Table 1, our method achieves the highest F1-score compared with other methods, and the AUC is higher than 9 models. To be specific, compared with DRIU (Maninis et al., 2016) and BTS-DSN (Guo et al., 2019) which need only one forward pass to generate the segmentation map during testing, our method achieves much higher Se, Acc, AUC, and F1. Specifically, the Acc and AUC of our method are about 0.2% higher than DRIU and BTS-DSN. Besides,

Table 1 Comparison results on the DRIVE dataset (For each metric, the best results are shown in bold.)

Method	One Forward Pass?	Se	Sp	Acc	AUC	F1	SSIM	PSNR	fps	Params(M)
Liskowski et al. (Liskowski and Krawiec, 2016)	No	0.7811	0.9807	0.9535	0.9790	N.A	N.A	N.A	N.A	N.A
FCN (Oliveira et al., 2018)	No	0.8039	0.9804	0.9576	0.9821	N.A	N.A	N.A	0.5	0.2
U-Net (Jin et al., 2019)	No	0.7849	0.9802	0.9554	0.9761	0.8175	N.A	N.A	0.32	3.4
DUNet (Jin et al., 2019)	No	0.7963	0.9800	0.9566	0.9802	0.8237	N.A	N.A	0.07	0.9
DEU-Net (Wang et al., 2019a)	No	0.7940	0.9816	0.9567	0.9772	0.8270	N.A	N.A	0.15	N.A
MS-NFN (Wu et al., 2018)	No	0.7844	0.9819	0.9567	0.9807	N.A	N.A	N.A	0.1	0.4
Patch BTS-DSN (Guo et al., 2019)	No	0.7891	0.9804	0.9561	0.9806	0.8249	0.5159	13.5640	N.A	7.8
Three-stage FCN (Yan et al., 2018b)	No	0.7631	0.9820	0.9538	0.9750	N.A	N.A	N.A	N.A	20.4
Vessel-Net (Wu et al., 2019)	No	0.8038	0.9802	0.9578	0.9821	N.A	N.A	N.A	N.A	1.7
DRIU (Maninis et al., 2016)	Yes	0.7855	0.9799	0.9552	0.9793	0.8220	0.5923	13.6364	N.A	7.8
Image BTS-DSN (Guo et al., 2019)	Yes	0.7800	0.9806	0.9551	0.9796	0.8208	0.5941	14.2633	N.A	7.8
Our Method	Yes	0.7934	0.9810	0.9571	0.9816	0.8289	0.5500	13.7672	11.8	0.1

¹ N.A : Not Available**Table 2** Comparison results on the CHASE_DB1 dataset (For each metric, the best results are shown in bold.)

Method	One Forward Pass?	Se	Sp	Acc	AUC	F1	SSIM	PSNR	fps	Split of dataset
MS-NFN (Wu et al., 2018)	No	0.7538	0.9847	0.9637	0.9825	N.A	N.A	N.A	<0.1	20/8 (train/test)
Three-stage FCN (Yan et al., 2018b)	No	0.7641	0.9806	0.9607	0.9776	N.A	N.A	N.A	N.A	20/8 (train/test)
Vessel-Net (Wu et al., 2019)	No	0.8132	0.9814	0.9661	0.9860	N.A	N.A	N.A	N.A	20/8 (train/test)
Xu et al. (Xu et al., 2020)	No	N.A	N.A	0.9650	0.9856	N.A	N.A	N.A	N.A	20/8 (train/test)
DEU-Net (Wang et al., 2019a)	No	0.8074	0.9821	0.9661	0.9812	0.8037	N.A	N.A	0.08	20/8 (train/test)
BTS-DSN (Guo et al., 2019)	Yes	0.7888	0.9801	0.9627	0.9840	0.7983	0.6052	14.2717	N.A	20/8 (train/test)
Our Method	Yes	0.7839	0.9842	0.9660	0.9860	0.8124	0.6602	14.4583	5.6	20/8 (train/test)
U-Net (Jin et al., 2019)	No	0.8355	0.9698	0.9578	0.9784	0.7792	N.A	N.A	0.10	14/14 (train/test)
DUNet (Jin et al., 2019)	No	0.8155	0.9752	0.9610	0.9804	0.7883	N.A	N.A	0.02	14/14 (train/test)
Our Method	Yes	0.7645	0.9846	0.9650	0.9840	0.8021	0.6985	14.7485	5.6	14/14 (train/test)

¹ N.A : Not Available**Table 3** Comparison results on the HRF dataset (For each metric, the best results are shown in bold.)

Method	Se	Sp	Acc	AUC	F1	SSIM	PSNR
Orlando et al. (Orlando et al., 2016)	0.7874	0.9584	N.A	N.A	0.7158	N.A	N.A
Zhao et al. (Zhao et al., 2017)	0.7490	0.9420	0.9410	0.9710	N.A	N.A	N.A
Yan et al. (Yan et al., 2018a)	0.7881	0.9592	0.9437	N.A	N.A	N.A	N.A
Our Method	0.7926	0.9764	0.9591	0.9697	0.7835	0.3062	13.0284

¹ N.A : Not Available

compared with the other eight methods that need multiple forward passes to generate the segmentation map during testing for only one fundus image, the Se, Acc, Auc, and F1 of our method is higher than six of the eight methods.

On the CHASE_DB1 dataset, we compare our method with eight existing methods. Our method achieves the highest AUC and F1 compared with other state-of-the-art methods, as can be seen in Table 2. Besides, compared with U-Net and its variant models, namely DUNet and DEU-Net, our method shows superior performance in terms of Sp, AUC, and F1-score.

Besides adopting pixel-wise evaluation metrics, we also report the SSIM and PSNR of our method. We can observe that the SSIM and PSNR of our method outperform BTS-DSN on the CHASE_DB1 datasets by a significant margin. To be specific, the SSIM of DPN is over 5.5% higher than that of BTS-DSN. On the DRIVE dataset, the PSNR of our method is better than that of

Patch BTS-DSN and DRIU, but lower than Image BTS-DSN. Although Image BTS-DSN achieves better SSIM and PSNR, its acc and AUC are lower than our method. We conclude that our method still shows competitive performance in terms of SSIM and PSNR.

At last, on the HRF dataset, our method also shows its superior performance compared with other methods. This part of the experiments real that our method achieves comparable or even superior performance in segmentation performance.

Segmentation speed. On the DRIVE dataset, the fps of our method is over 10, while the fps of all state-of-the-art methods are lower than 1.0. For instance, the segmentation speed of our method is over $20\times$, $100\times$ faster than FCN (Oliveira et al., 2018) and MS-NFN (Wu et al., 2018), respectively.

On the CHASE_DB1 dataset, most existing state-of-the methods require multiple forward passes and a recomposed operation to generate a segmentation map for one fundus image, thus they show slow segmentation speed. Compared with DUNet (Jin et al., 2019) and DEU-Net (Wang et al., 2019a), they need over 10s to segment a fundus image with resolution 999×960 . However, our method runs in an end-to-end way, and it could segment an image within 0.2s, which is over $280\times$ and $70\times$ faster than DUNet and DEU-Net.

We conclude that our method has obvious advantages in segmentation speed, which could better meet the real-time requirement in a clinical scene.

Number of parameters. The number of parameters of our model is only 120k, which is far less than all state-of-the-art models. Therefore, our method is more suitable to be deployed to edge devices due to its lightweight characteristic.

4.5.2 Visualization

To show the effectiveness of our proposed DPN, we present the segmentation probability maps and the corresponding binary maps in Fig. 6. We can observe that our model could detect both thin vessels and thick vessel trees, verifying the effectiveness of our proposed DP-Block.

Moreover, we present several challenging cases in Fig. 7. We can observe that our model could detect thin vessels with only one-pixel width, as DPN always preserves the spatial information. In addition, our model is able to segment some extremely thin vessels with low contrast near the macula. In the third row of Fig. 7, there exist two lumps of hemorrhage, which shares similar local features with vessels. As the DPN could capture structural information, as a result, the DPN is robust to the presence of hemorrhages. Also, for some true vessels not annotated, our model could segment well. In summary, the proposed method could segment thick and thin vessels, and robust to noise.

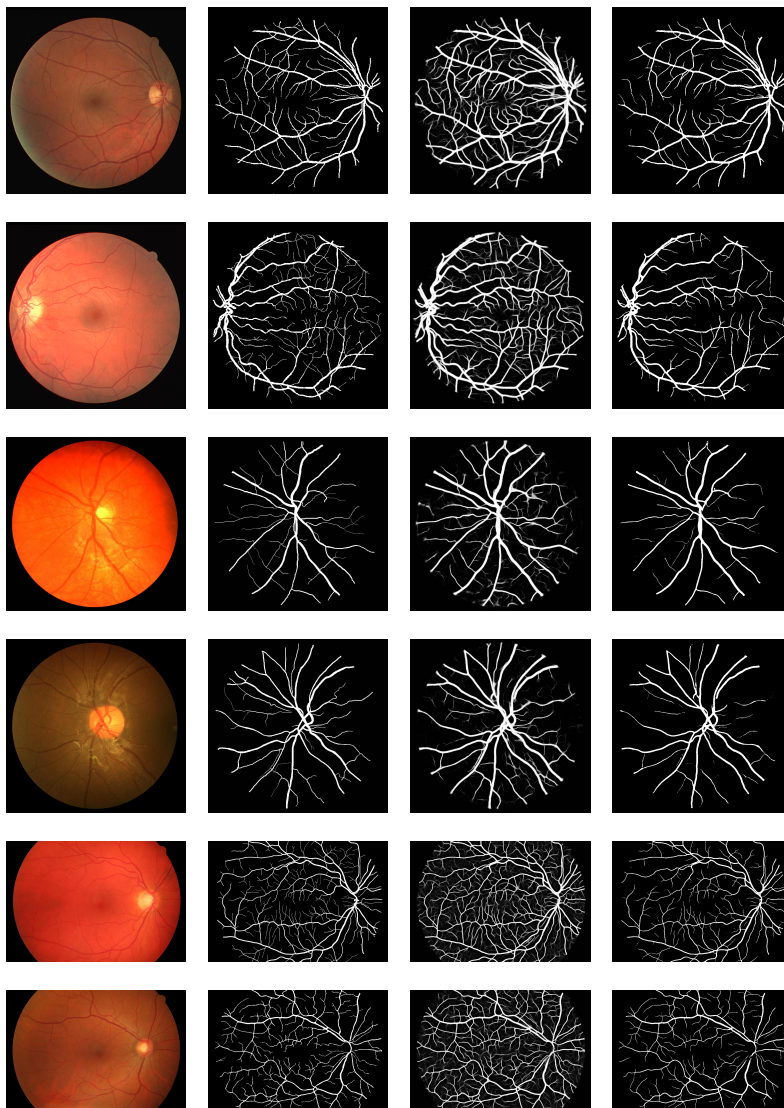


Fig. 6 Visualization of the segmentation maps. From columns 1 to 4: fundus images, ground truth, probability maps, and binary maps.

4.6 Ablation Study

4.6.1 Effectiveness of Auxiliary Losses

In order to verify the impact of auxiliary losses on the final segmentation performance of the model, we removed all three auxiliary losses in DPN and the model was trained again under the same settings. The experimental results



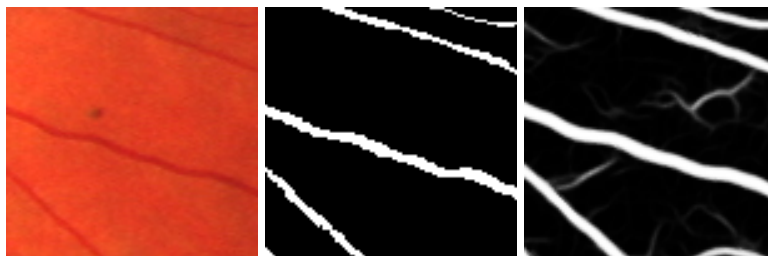
(a) Segmentation of extremely thin vessels



(b) Segmentation of low-contrast vessels



(c) Segmentation in the presence of hemorrhages



(d) Segmentation in the presence of microaneurysms

Fig. 7 Visualization of some challenging cases. From left to right: fundus images patches, ground-truth, and the segmentation probability maps generated by proposed DPN.

Table 4 Comparison results of employing auxiliary losses or not (best results shown in bold).

Dataset	Auxiliary Loss?	Se	Sp	Acc	AUC	F1
DRIVE	No	0.7874	0.9810	0.9564	0.9808	0.8259
	Yes	0.7934	0.9810	0.9571	0.9816	0.8289
CHASE_DB1	No	0.7805	0.9833	0.9649	0.9840	0.8058
	Yes	0.7839	0.9842	0.9660	0.9860	0.8124
HRF	No	0.7887	0.9759	0.9583	0.9679	0.7792
	Yes	0.7926	0.9764	0.9591	0.9697	0.7835

Table 5 Comparison results of multi-scale feature fusion in DP-Block (OS is short for output stride, and OS1/OS2/OS4 corresponds to the first/second/third branch of DP-Block, respectively)

Dataset	Feature Fusion	Se	Sp	Acc	AUC	F1	SSIM	PSNR
DRIVE	OS1	0.7875	0.9813	0.9566	0.9808	0.8262	0.5303	13.8216
	+OS2	0.7874	0.9816	0.9569	0.9810	0.8277	0.5093	13.5204
	+OS2+OS4	0.7934	0.9810	0.9571	0.9816	0.8289	0.5500	13.7672
CHASE_DB1	OS1	0.7631	0.9843	0.9642	0.9826	0.8015	0.5507	14.1293
	+OS2	0.7684	0.9841	0.9645	0.9838	0.8035	0.5379	13.4846
	+OS2+OS4	0.7839	0.9842	0.9660	0.9860	0.8124	0.6602	14.4583

were summarized in Table 4. We can observe that almost all evaluation metrics were decreased after removing auxiliary losses. Specifically, the F1-score was decreased over 0.3% on all three datasets. This part of the experiments verifies the rationality and effectiveness of adopting auxiliary losses in DPN.

4.6.2 Effectiveness of Multi-scale Feature Fusion in DP-Block

In order to verify the effectiveness of multi-scale feature fusion in DP-Block, we conduct three groups of experiments, i.e., the DP-Block contains only the first branch, the DP-Block contains the first and the second branch, and the DP-Block contains all of three branches. Experimental results are summarized in Table 5. We can observe that, after adding the second and the third branch, the segmentation performance has been improved over DRIVE and CHASE_DB1 datasets. To be specific, the F1-score of DPN with three branches is over 1.09% higher than that of DPN with only the first branch. This part of the experiments reveals that it is necessary to adopt multi-scale feature fusion within DP-Block.

4.6.3 The Number of Convolutional Filters

Table 6 demonstrates the ablation results of various number of convolutional filters. First, setting C0, C1, and C2 to 16, 8, 8 for each DP-Block outperforms other configurations over DRIVE and CHASE_DB1 datasets. Second, improving segmentation speed, that is, such thin convolutional filters can significantly accelerate inference speed. Third, thick convolutional filters mean

Table 6 Ablation studies on the number of convolutional filters.

Dataset	C0	C1	C2	Se	Sp	Acc	AUC	F1	SSIM	PSNR
DRIVE	8	4	4	0.7894	0.9802	0.9559	0.9806	0.8242	0.5150	13.7664
	8	8	8	0.7840	0.9815	0.9563	0.9808	0.8254	0.5141	13.7618
	16	8	8	0.7934	0.9810	0.9571	0.9816	0.8289	0.5500	13.7672
	24	12	12	0.7942	0.9808	0.9571	0.9813	0.8283	0.5023	13.5176
CHASE_DB1	8	4	4	0.7563	0.9846	0.9639	0.9833	0.7998	0.5620	13.8856
	8	8	8	0.7485	0.9845	0.9631	0.9820	0.7950	0.5703	14.3965
	16	8	8	0.7839	0.9842	0.9660	0.9860	0.8124	0.6602	14.4583
	24	12	12	0.7747	0.9835	0.9645	0.9838	0.8045	0.5215	13.5914

high memory consumption and high optimization difficulty. At last, considering the trade-off between segmentation accuracy and inference speed, we set C0, C1, and C2 to 16, 8, and 8 in DP-Block.

5 Conclusion

Deep learning models have been applied to retinal vessel segmentation in recent years, and achieve remarkable performance. In this paper, we propose a deep model, called DPN to segment retinal vessel trees. Different from U-Net and FCN, in which detailed spatial information is sacrificed to learn structured information. Our method could preserve the detailed information all the time via maintaining a high resolution throughout the whole process, benefiting locating the vessel boundaries accurately. To accomplish this goal, we present the DP-Block further, where multi-scale fusion is adopted to preserve both detailed information and learn structural information. In order to show the effectiveness of our method, DPN is trained from scratch over three publicly available datasets: DRIVE, CHASE_DB1, and HRF. Experimental results show that our method shows competitive/better performance in terms of F1-score and segmentation speed with only about 120k parameters. Specifically, the segmentation speed of our method is over 20-160 \times faster than other state-of-the-art methods on the DRIVE dataset. In summary, considering the segmentation accuracy, segmentation speed, and model size together, our model shows superior performance and is suitable for real-world application. Meantime, there are some drawbacks of DPN. For example, it cannot process high-resolution fundus images directly, and there are discontinuous vessel patches in the binary map. In the future, we aim to extend our method and develop robust deep models for fundus microaneurysms segmentation. At last, the source code of our method is available at <https://github.com/guomugong/DPN>.

Funding

This work is supported by PhD research startup foundation of Xi'an University of Architecture and Technology (No.1960320048).

Conflict of interest

The authors have no conflicts of interest to declare that are relevant to the content of this article.

Availability of data and material

All databases utilized in this publication are publicly available, namely DRIVE [Staal et al. \(2004\)](#), CHASE_DB1 [Fraz et al. \(2012\)](#), and HRF [Budai et al. \(2013\)](#).

Code availability

The source code will be available at <https://github.com/guomugong/DPN>.

References

- Azzopardi G, Petkov N (2013) Automatic detection of vascular bifurcations in segmented retinal images using trainable cosfire filters. *Pattern Recognit Lett* 34(8):922–933, DOI 10.1016/j.patrec.2012.11.002
- Azzopardi G, Strisciuglio N, Vento M, Petkov N (2015) Trainable cosfire filters for vessel delineation with application to retinal images. *Med Image Anal* 19(1):46–57
- Budai A, Bock R, Maier A, Hornegger J, Michelson G (2013) Robust vessel segmentation in fundus images. *Int J of Biomed Imaging* 2013
- Cao L, Li H, Zhang Y, Zhang L, Xu L (2020) Hierarchical method for cataract grading based on retinal images using improved haar wavelet. *Inf Fusion* 53:196–208, DOI 10.1016/j.inffus.2019.06.022
- Christodoulidis A, Hurtut T, Tahar HB, Cheriet F (2016) A multi-scale tensor voting approach for small retinal vessel segmentation in high resolution fundus images. *Comput Med Imaging and Graph* 52:28–43, DOI 10.1016/j.compmedimag.2016.06.001
- Fraz MM, Remagnino P, Hoppe A, Uyyanonvara B, Rudnicka AR, Owen CG, Barman SA (2012) Blood vessel segmentation methodologies in retinal images - a survey. *Comput Methods and Programs in Biomed* 108(1):407–433, DOI 10.1016/j.cmpb.2012.03.009
- Fu H, Xu Y, Lin S, Wong DWK, Liu J (2016) Deepvessel: Retinal vessel segmentation via deep learning and conditional random field. In: *International Conference on Medical Image Computing and Computer-Assisted Intervention*, pp 132–139, DOI 10.1007/978-3-319-46723-8_16
- Garg S, Sivaswamy J, Chandra S (2007) Unsupervised curvature-based retinal vessel segmentation. In: *IEEE International Symposium on Biomedical Imaging: From Nano to Macro, IEEE*, pp 344–347, DOI 10.1109/ISBI.2007.356859

- Glorot X, Bengio Y (2010) Understanding the difficulty of training deep feed-forward neural networks. In: International Conference on Artificial Intelligence and Statistics (AISTATS), PMLR, Proceedings of Machine Learning Research, vol 9, pp 249–256
- Guo S, Wang K, Kang H, Zhang Y, Gao Y, Li T (2019) Bts-dsn: Deeply supervised neural network with short connections for retinal vessel segmentation. *Int J of Med Inform* 126:105–113, DOI 10.1016/j.ijmedinf.2019.03.015
- Irshad S, Akram MU (2014) Classification of retinal vessels into arteries and veins for detection of hypertensive retinopathy. In: Cairo International Biomedical Engineering Conference (CIBEC), IEEE, pp 133–136
- Jia Y, Shelhamer E, Donahue J, Karayev S, Long J, Girshick R, Guadarrama S, Darrell T (2014) Caffe: Convolutional architecture for fast feature embedding. In: ACM International Conference on Multimedia, pp 675–678, DOI 10.1145/2647868.2654889
- Jin Q, Meng Z, Pham TD, Chen Q, Wei L, Su R (2019) Dunet: A deformable network for retinal vessel segmentation. *Knowledge-Based Syst* 178:149–162, DOI 10.1016/j.knosys.2019.04.025
- Kingma DP, Ba JL (2015) Adam: a method for stochastic optimization. In: International Conference on Learning Representations, pp 1–13
- Lee CY, Xie S, Gallagher P, Zhang Z, Tu Z (2015) Deeply-Supervised Nets. In: International Conference on Artificial Intelligence and Statistics, Proceedings of Machine Learning Research, vol 38, pp 562–570, URL <http://proceedings.mlr.press/v38/lee15a.html>
- Li Q, You J, Zhang L, Bhattacharya P (2006) A multiscale approach to retinal vessel segmentation using gabor filters and scale multiplication. In: IEEE International Conference on Systems, Man and Cybernetics, IEEE, vol 4, pp 3521–3527, DOI 10.1109/ICSMC.2006.384665
- Liskowski P, Krawiec K (2016) Segmenting retinal blood vessels with deep neural networks. *IEEE Trans on Med Imaging* 35(11):2369–2380, DOI 10.1109/TMI.2016.2546227
- Maninis KK, Pont-Tuset J, Arbeláez P, Van Gool L (2016) Deep retinal image understanding. In: International Conference on Medical Image Computing and Computer-Assisted Intervention, pp 140–148, DOI 10.1007/978-3-319-46723-8_17
- Mookiah MRK, Hogg S, MacGillivray TJ, Prathiba V, Pradeepa R, Mohan V, Anjana RM, Doney AS, Palmer CN, Trucco E (2020) A review of machine learning methods for retinal blood vessel segmentation and artery/vein classification. *Med Image Anal* p 101905
- Oliveira A, Pereira S, Silva CA (2018) Retinal vessel segmentation based on fully convolutional neural networks. *Expert Syst with Appl* 112:229–242, DOI 10.1016/j.eswa.2018.06.034
- Orlando JI, Prokofyeva E, Blaschko MB (2016) A discriminatively trained fully connected conditional random field model for blood vessel segmentation in fundus images. *IEEE Trans on Biomed Eng* 64(1):16–27
- Ronneberger O, Fischer P, Brox T (2015) U-net: Convolutional networks for biomedical image segmentation. In: International Conference on Medical

- Image Computing and Computer-Assisted Intervention, Springer, pp 234–241, DOI 10.1007/978-3-319-24574-4_28
- Saleh MD, Eswaran C, Mueen A (2011) An automated blood vessel segmentation algorithm using histogram equalization and automatic threshold selection. *J of Digit Imaging* 24(4):564–572
- Schmidt-Erfurth U, Sadeghipour A, Gerendas BS, Waldstein SM, Bogunović H (2018) Artificial intelligence in retina. *Prog in Retin and Eye Res* 67:1–29, DOI 10.1016/j.preteyeres.2018.07.004
- Scott IU, Alexandrakis G, Cordahi GJ, Murray TG (1999) Diffuse and circumscribed choroidal hemangiomas in a patient with sturge-weber syndrome. *Arch of Ophthalmol* 117(3):406–407
- Shelhamer E, Long J, Darrell T (2017) Fully convolutional networks for semantic segmentation. *IEEE Trans on Pattern Anal and Mach Intell* 39(4):640–651, DOI 10.1109/TPAMI.2016.2572683
- Srinidhi CL, Aparna P, Rajan J (2017) Recent advancements in retinal vessel segmentation. *J of Med Syst* 41(4):70
- Srinidhi CL, Aparna P, Rajan J (2018) A visual attention guided unsupervised feature learning for robust vessel delineation in retinal images. *Biomed Signal Process and Control* 44:110–126
- Staal J, Abràmoff MD, Niemeijer M, Viergever MA, Van Ginneken B (2004) Ridge-based vessel segmentation in color images of the retina. *IEEE Trans on Med Imaging* 23(4):501–509, DOI 10.1109/tmi.2004.825627
- Szegedy C, Liu W, Jia Y, Sermanet P, Reed S, Anguelov D, Erhan D, Vanhoucke V, Rabinovich A (2015) Going deeper with convolutions. In: *IEEE Conference on Computer Vision and Pattern Recognition*, pp 1–9, DOI 10.1109/CVPR.2015.7298594
- Villalobos-Castaldi FM, Felipe-Riverón EM, Sánchez-Fernández LP (2010) A fast, efficient and automated method to extract vessels from fundus images. *J of Vis* 13(3):263–270
- Wang B, Qiu S, He H (2019a) Dual encoding u-net for retinal vessel segmentation. In: *International Conference on Medical Image Computing and Computer-Assisted Intervention*, Springer, pp 84–92, DOI 10.1007/978-3-030-32239-7_10
- Wang J, Sun K, Cheng T, Jiang B, Deng C, Zhao Y, Liu D, Mu Y, Tan M, Wang X, et al. (2020) Deep high-resolution representation learning for visual recognition. *IEEE Trans on Pattern Anal and Mach Intell* DOI 10.1109/TPAMI.2020.2983686
- Wang W, Wang W, Hu Z (2019b) Retinal vessel segmentation approach based on corrected morphological transformation and fractal dimension. *IET Image Process* 13(13):2538–2547
- Wang X, Jiang X, Ren J (2019c) Blood vessel segmentation from fundus image by a cascade classification framework. *Pattern Recognit* 88:331–341, DOI 10.1016/j.patcog.2018.11.030
- Wang Y, Ji G, Lin P, Trucco E (2013) Retinal vessel segmentation using multi-wavelet kernels and multiscale hierarchical decomposition. *Pattern Recognit* 46(8):2117–2133, DOI 10.1016/j.patcog.2012.12.014

- Wang Z, Bovik AC, Sheikh HR, Simoncelli EP (2004) Image quality assessment: from error visibility to structural similarity. *IEEE Trans on Image Process* 13(4):600–612
- Wong TY, Coresh J, Klein R, Muntner P, Couper DJ, Sharrett AR, Klein BE, Heiss G, Hubbard LD, Duncan BB (2004) Retinal microvascular abnormalities and renal dysfunction: the atherosclerosis risk in communities study. *J of the Am Soc of Nephrol* 15(9):2469–2476, DOI 10.1097/01.ASN.0000136133.28194.E4
- Wong TY, Sun J, Kawasaki R, Ruamviboonsuk P, Gupta N, Lansingh VC, Maia M, Mathenge W, Moreker S, Muqit MM, et al. (2018) Guidelines on diabetic eye care: the international council of ophthalmology recommendations for screening, follow-up, referral, and treatment based on resource settings. *Ophthalmol* 125(10):1608–1622, DOI 10.1016/j.ophtha.2018.04.007
- Wu Y, Xia Y, Song Y, Zhang Y, Cai W (2018) Multiscale network followed network model for retinal vessel segmentation. In: *International Conference on Medical Image Computing and Computer-Assisted Intervention*, pp 119–126, DOI 10.1007/978-3-030-00934-2_14
- Wu Y, Xia Y, Song Y, Zhang D, Liu D, Zhang C, Cai W (2019) Vessel-net: retinal vessel segmentation under multi-path supervision. In: *International Conference on Medical Image Computing and Computer-Assisted Intervention*, Springer, pp 264–272, DOI 10.1007/978-3-030-32239-7_30
- Xie S, Tu Z (2017) Holistically-nested edge detection. *Int J of Comput Vision* 125(1-3):3–18, DOI 10.1007/s11263-017-1004-z
- Xu R, Ye X, Jiang G, Liu T, Li L, Tanaka S (2020) Retinal vessel segmentation via a semantics and multi-scale aggregation network. In: *IEEE International Conference on Acoustics, Speech and Signal Processing (ICASSP)*, IEEE, pp 1085–1089
- Yan Z, Yang X, Cheng KT (2018a) Joint segment-level and pixel-wise losses for deep learning based retinal vessel segmentation. *IEEE Trans on Biomed Eng* 65(9):1912–1923
- Yan Z, Yang X, Cheng KT (2018b) A three-stage deep learning model for accurate retinal vessel segmentation. *IEEE J of Biomed and Health Inform* 23(4):1427–1436, DOI 10.1109/JBHI.2018.2872813
- Yin Y, Adel M, Bourennane S (2012) Retinal vessel segmentation using a probabilistic tracking method. *Pattern Recognit* 45(4):1235–1244, DOI 10.1016/j.patcog.2011.09.019
- Yu H, Barriga S, Agurto C, Zamora G, Bauman W, Soliz P (2012) Fast vessel segmentation in retinal images using multi-scale enhancement and second-order local entropy. In: *Medical imaging 2012: computer-aided diagnosis*, International Society for Optics and Photonics, SPIE, pp 386 – 397
- Zhao Y, Zheng Y, Liu Y, Zhao Y, Luo L, Yang S, Na T, Wang Y, Liu J (2017) Automatic 2-d/3-d vessel enhancement in multiple modality images using a weighted symmetry filter. *IEEE Trans on Med Imaging* 37(2):438–450